Aerosol-Jet Printed and Photonically Cured Sensors Embedded in 3D Printed Smart Orthoses: A Preliminary Study

Lorenzo Rossetti
Information Engineering Department
Università degli Studi di Brescia
Brescia, Italy
l.rossetti005@unibs.it

Michela Borghetti
Information Engineering Department
Università degli Studi di Brescia
Brescia, Italy
michela.borghetti@unibs.it

Mauro Serpelloni
Information Engineering Department
Università degli Studi di Brescia
Brescia, Italy
mauro.serpelloni@unibs.it

***Abstract*—Enhancing 3D printed objects with embedded electronics is an increasing need and opportunity in the field of Internet of Things (IoT), Biomedical applications and Industry 4.0. 3D printed prostheses are emerging rapidly, embedding sensors in them can enable monitoring during recovery phases or long term to assess their integrity without modifying structure or patient's experience. In this work, a first example of strain gauge embedded inside a 3D printed structure realized with AJP and photonic curing is presented. Commercially available printer and material such as PLA are considered in this preliminary study. To produce the proof-of-concept samples, the 3D printing process was initiated and paused at a certain layer, which was post produced by the printer itself using ironing technique, then the sensor was printed by Aerosol Jet Printing technique using a silver nanoparticulate ink, which was then cured via photonic sintering; finally, the 3D printing process was resumed to complete the structure. A set of not embedded sensors were used to validate the sensors' fabrication process and sensing capabilities. Post processed surface and sensors were characterized morphologically using a profilometer, resulting in a surface with average roughness of 0.72 µm (89% less than non-ironed surface) and a homogenous track width of 200 µm. Flexural 3-Point bending tests were conducted to measure electrical response. Sensitivity in 3-Point bending tests was found to be 0.87 ± 0.12 $(\Omega/\Omega)/\varepsilon$ with R^2 of 0.98 minimum. Proof-of-concept embedded strain sensors were subjected also to flexural testing and validated the feasibility of the process.**

Keywords—Aerosol jet printing, additive manufacturing, 3D printing, embedded sensing, prosthesis, strain measurement.

I. Introduction

Over the past decade, additive manufacturing (AM) has emerged as a transformative technology in orthotics and prosthetics, enabling faster, more cost-effective, and highly customizable device fabrication compared to traditional processes. Clinical outcomes have demonstrated improved fit, comfort, effectiveness, and patient satisfaction for 3D-printed, patient-specific ankle-foot orthoses (AFOs), knee-ankle-foot orthoses (KAFOs), and insoles [1].

Alongside advances in fabrication, the development of monitoring systems to enhance rehabilitation and long-term assistance has become an increasingly active area of research. Various sensing approaches have been explored for orthosis monitoring, ranging from compliance assessment to the measurement of loads, joint kinematics, and gait parameters. Compliance monitoring systems reported in the literature typically rely on temperature sensors, pressure sensors, accelerometers, or combinations thereof [2]. For kinematic monitoring, Oracea et al. [3] demonstrated the integration of inertial measurement units (IMUs) into a 3D-printed KAFO to provide corrective feedback for total knee arthroplasty (TKA) patients during post-operative recovery. Piezoresistive sensing for kinematic measurement has also been investigated, both using conventional materials [4][5] and textile-based substrates [6], while strain gauges represent a further viable solution. For example, Papi et al. [7] demonstrated a preliminary study on classical strain gauges applied to an AFO to measure sagittal plane angles, showing repeatable gait cycles data. Furthermore, Dufek et al. [8] proposed an 8-sensor system that shows how gait analysis gathered from strain gauges data can provide insights about the effect of orthoses on patients with Charcot–Marie–Tooth (CMT).

In most cases, however, these sensors were applied externally to the orthotic structure after fabrication, introducing additional assembly steps and potential reliability concerns. Embedding sensing elements directly within additively manufactured orthoses represents a promising strategy to address these limitations. Integrated sensors can reduce assembly complexity, improve mechanical robustness, and enable more compact, patient-specific designs. Several approaches have been explored in the literature [9]. A simple method is fitting commercially available sensors or electronic components during printing; Shemelya et al.[10], show a whole system of printed and commercial off-the shelf (COTS) sensors embedded inside a 3D printed encapsulation for the aerospace field. Multi-material printing of insulating and conductive materials via fused deposition modelling (FDM) is an alternative that is attracting increasing attention; Stano et al. [11], for example, demonstrated an orthotic finger with embedded strain sensors fabricated using conductive PLA. Even though this approach grants a more efficient process when creating the whole structure, sensing elements are limited in geometry and resolution. Alternative strategies incorporate additional deposition processes within the AM workflow, such as aerosol jet printing (AJP) [12], direct ink writing (DIW), or inkjet printing [13], effectively decoupling sensor fabrication from the structural print while maintaining a unified manufacturing workflow. Feature resolution at the tens of microns scale and material flexibility are offered by this hybrid approach.

While AJP has been widely applied to conformal printing on complex surfaces, its integration within the FDM fabrication cycle as an embedded sensing strategy has received little attention, representing a gap this work aims to address. A novel one-shot sensorization strategy for orthotic structures during manufacturing is proposed. A commercially available FDM printer was employed using polylactic acid (PLA) as the substrate material. The process follows a Print-Pause-Print (PPP) approach [14]: printing is automatically paused at a predefined layer, aerosol jet printing is used to deposit the sensor traces, the ink is dried in a low-pressure oven and photonically sintered, and printing is then resumed to completion. To ensure adequate surface quality for AJP deposition, a post-processing step known as ironing was applied during 3D printing, whereby the heated nozzle flattens the top surface and reduces roughness to below 1 µm, sufficient for ink layers of 4 to 5 µm thickness [15], [16]. To evaluate the feasibility of the proposed process and the sensing performance of the embedded elements, bending specimens were fabricated and experimentally characterized. Strain gauges were first printed onto the 3D-printed substrate and tested under flexural loading. Subsequently, modified specimens with additional printed layers deposited over the sensors were produced to achieve full structural embedding and tested under equivalent mechanical conditions.

II. Materials and Methods

A. Fabrication Process

The objective of this work is to embed aerosol-jet printed strain sensors directly within the structure of additively manufactured orthoses — such as AFOs — during the FDM fabrication process, enabling a fully integrated, patient-specific sensorized device (Fig. 1). As a preliminary step toward this goal, the feasibility of the proposed PPP-based embedding technique is assessed on standardized bending specimens, which allow controlled mechanical characterization of the sensor response under flexural loading. The fabrication workflow and the embedding process are illustrated in Fig. 2. The materials, manufacturing parameters, and experimental procedures adopted in this study are described in the following sections.

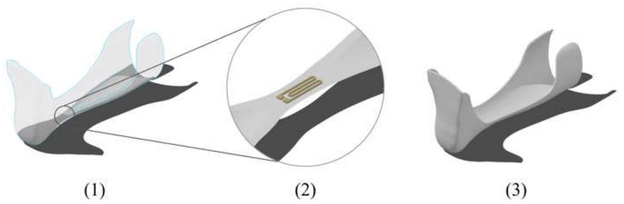

Fig. 1. AFO concept fabrication workflow. 3D-print up to a layer (1) at which ironing is applied, sensor fabrication (2) during 3D-printing pause, resuming and finishing 3D-printing of the full structure.

A linear strain gauge was designed to be tested and embedded inside the 3D printing structure. The design is a simple meander of tracks with grid width of 5.7 mm and length of 6 mm. Two pads were also designed at the ends to help contacting wires.

Test specimens and proof of concept device were fabricated using 3D printing. Sensors were deposited on their cured surface, by means of Aerosol Jet Printing technique. The deposition was cured through a photonic sintering. Finally, sensors were contacted with a conductive epoxy. A set of 10 samples were created to test fabrication process and sensing properties, without embedding them. Two samples were then embedded with two additional layers of PLA as proof-of-concept devices.

A commercially available 3D printer (BambuLab X1C) was employed to produce the substrates made from PLA filament (BambuLab). A 0.4 mm brass nozzle was used, layer height was set to 0.2 mm, while other printing parameters were left as default in accordance with manufacturer's technical datasheet. On the layer where sensors were deposited, ironing technique was employed. This way a low roughness surface was obtained, which granted continuous AJP depositions. In this process, the hot tool head passes over this layer again while extruding a given amount of material at a set speed and with tight line spacing. For every sample presented in this work, parameters were set as follows: ironing speed of 30 mm/s, flow of 15% of material and 0.1 mm of line spacing. The printing process was paused at the designed layer to allow sensors fabrication. The whole plate with unfinished objects was then transferred to the Optomec AJ-300 printer where sensors were printed on the substrates' cured surface. A silver ink by GenesInk was used. The ink is based on silver nanoparticulate.

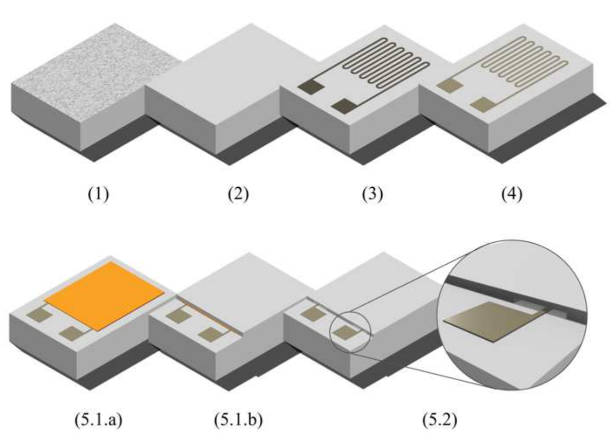

Fig. 2. Fabrication process used to produce test specimens (1-4) and proof-of-concept devices (1-5). 3D printing to a certain layer (1), the surface is ironed (2), AJP deposition of silver nanoparticulate to produce sensor (3) and photonic curing to finalize sensor (4). Final structure using 3D printing (5) is produce following two alternative approaches: steps (5.1a–5.1.b) where kapton tape is placed to cover AJP tracks before continuing printing or step (5.2) where the following layer don't touch but remain hovering on the surface modelling a cave.

The deposition was performed using a nozzle of 750 µm. The printing speed was set to 2 mm/s and were deposited 4 layers of material for each sensor. The heated plate was set to 55 °C to keep PLA adherent to its 3D printer plate and allow for quick drying of the ink while deposited.

TABLE I. Aerosol Jet Printing Parameters

Parameter	Values	
	Flow (SCCM)	*Pressure (psi)*
Sheath	1200	0.272
Atomizer	580	2.466
Extractor	560	0.141

After AJP deposition, all samples were dried at 50 °C for 8 hours at low pressure, to let ethanol and additives evaporate.

Ink depositions were then cured using a photonic sintering tool Pulse Forge 1300 by Novacentrix. The technique was employed to avoid exposing PLA to high temperatures during curing, normally this ink sinters at 180 °C. A train of pulses with amplitude of 350 V, at 25% of duty cycle each, carried by an exponential envelope with 5 ms in duration, was repeated for 12 times to ensure sintering of the nanoparticulate. TABLE II. sums all sintering parameters. These parameter values were selected after an empirical and brief design over experiment. Samples for photonic parameters optimization were created before and were sintered at different envelope times, voltage and duty cycle % to find a balance between reaching resistivity compared to literature values and avoiding PLA thermal dilation effects on the tracks. The substrates, as illustrated in following sections, has peaks and valleys on its surface comparable to AJP deposition thickens. Once heated by the photonic process, these peaks depart from each other and microscopic level. If not controlled this phenomenon can ultimately crack the tracks while curing which leads to device destruction. So, parameters were tuned to lower resistivity as much as possible before cracking the devices.

After photonic curing, the plate with unfinished objects was reinstalled inside the 3D printer to deposited 2 more layers on top of the sensors. Two methods of encapsulation were tried to avoid the hot tool head scratching the ink depositions: the first by placing a KAPTON tape piece on top of the sensor and then print directly, the second by creating in CAD a sort of cave to allow a 1-layer separation between sensor and next PLA printed.

All fabricated sensors were contacted with lead wires for testing with a conductive epoxy (Chemtronics® CW2400) and cured for 5 hours at 50°C. Two wires per pad were connected to the sensors to enable a 4-wire resistance measurement.

TABLE II. PHOTONIC CURING PARAMETERS

Parameter	Values
Voltage (V)	350
Envelope (μs)	5000
Duty Cycle (%)	25%
N. Pulses	7
Repeats	12
Energy Density (J/cm^2)	1.82
Distance (cm)	1.5

B. *Process Evaluation*

A Profilm3D profilometer made by Filmetrics was used to measure both surface treatment effect and cured ink deposition.

To evaluate ironing effect, samples were scanned in one location. Roughness was evaluated by extracting 10 line cuts of the total surface profilometry in 10 different places on the substrate. Considered parameters were average roughness R_a, root mean square roughness R_q, and mean roughness depth R_z. These were calculated considering two different frequency regimes, one using all frequencies from raw data and one considering only low frequencies, i.e., waviness, applying a Gaussian filter with L_C = 80 μm. The average of the 10 measures per parameter per frequency regime was used as result. Considering both raw data and waviness helps indicate if a substrate in printable or not using AJP ink deposition.

Sensors' morphology after deposition and sintering was evaluated with profilometry and microscopy. Track width and homogeneity was evaluated scanning one sample sensor in 4 different places. A line cut perpendicular to the tracks was taken in consideration in each place.

C. *Flexural tests*

Characterization of printed sensors was conducted with a flexural test. Sensors were printed in the center of the upper surface of a flat rectangular specimen for bending tests, a beam of 3.6 mm in thickness, 10 mm in width and 80 mm in length. An ESM1500 Mark-10® dynamometer was used to apply deflection to the specimen and thus strain the sensors and their electrical resistance response was measured via a $6_{½}$ digits digital multimeter Keysight® 34460A in a 4-wire configuration. Substrate specimens were designed in CAD with physical dimensions reported in the PLA's technical datasheet given by manufacturer and then printed according to previously explained process.

Flexural tests were conducted in a 3-point setup with rollers as points of contact with the specimen. The support span was set to 50 mm. Sensors were put face down underneath the moving roller, this way the application of bending caused an approximately linear tensile strain on the most external surface where the sensor is placed.

As preliminary test a commercially available strain gauge was applied to the surface of a flexural specimen with same properties as those used subsequently, to estimate substrate's Young's flexural modulus. The sensor used a linear strain gauge with a baseline resistance of 120 Ω. The beam was loaded and unloaded for 10 cycles controlling the machine in deflection from 0 to -1.2 mm along the z-axis with a constant speed of 1.2 mm/min and measuring the applied load with the integrated load cell in the dynamometer. The resistance response of the strain gauge was also measured.

Characterization of printed sensors was conducted on 9 test samples and 2 proof-of-concept devices. Similar loading history was applied to them. Given the results of the preliminary test, it was decided to subject these beams to a cycling deflection from 0 to -0.6 mm for 10 times. Force applied was measured, as well as sensors' electrical response. All tests were conducted at room temperature at approximately 22 °C without controlling both temperature and humidity.

III. RESULTS AND DISCUSSION

A. *Process Evaluation*

3D printed surfaces with no post-processing are visibly rough to the naked eye. Ink depositions with AJP are usually 1 to 2 μm high for each layer, so it's crucial to lower as much as possible surface roughness to ensure that sensors' traces could be continuous and so conductive, but also homogenous enough to sense strain correctly.

Raw data roughness R_a was measured at 0.72 μm and 6.35 μm from ironed and non-ironed surface respectively. Roughness from waviness, filtered by Gaussian filter with cut length of L_C = 80 μm, R_a was 0.48 μm and 1.87 μm for ironed and non-ironed surface respectively. Root mean square roughness also show improvements going from 7.46 μm and 2.99 μm (raw and waviness) to 0.90 μm and 0.59 μm (raw and waviness). Ultimately R_z went from 24.35 μm and 20.29 μm (raw and waviness) to 4.25 and 3.27 (raw and waviness). Fig. 3 shows a comparison of profilometer scans between the final ironed surface and a non-ironed one, with a cut line graph drawn perpendicularly to the main asperities of the substrate. Even though R_z was reduce significantly using ironing, a value around 3-4 μm is comparable with AJP deposition thickness. This can compromise photonic curing, which needs to be tuned carefully due to thermal dilation of PLA's crests, thus final adhesion, which compromises measuring performance of the strain sensors.

After AJP ink deposition and photonic sintering, samples' morphology was investigated to validate fabrication process. Fig. 4 shows a microscope capture of the full strain gauge geometry printed. A grid length of 6 mm and width of 5.7 mm was achieved as designed. In the inset, a first estimation of track width could be measured in 200 μm with a track spacing of 380 μm.

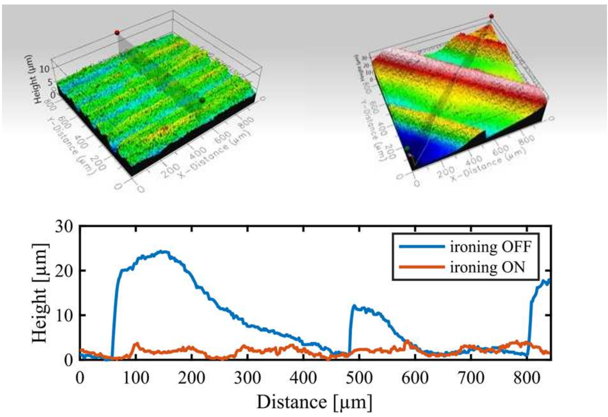

Fig. 3. 3D render of scan results from profilometry (above) of ironed (left) and non-ironed (right) surfaces. Line cut (below) of the profile of non-ironed (blu) and ironed (red) surfaces.

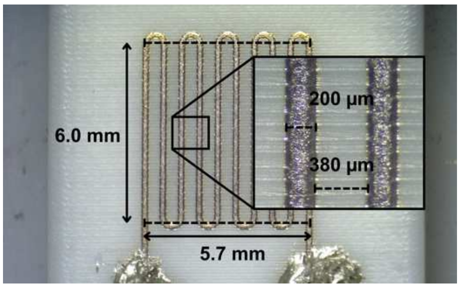

Fig. 4. Microscope capture of a strain gauge printed on PLA (x0.8 zoom) . In the inset a x5 magnification image of two parallel tracks.

Profilometry scans were used to assess more precisely the structure of substrate and sensor. Raw data from profilometer were filtered with a gaussian filter with cut length $L_C = 80$ µm. As shown in Fig. 5, track width and spacing is confirmed. Even though the substrate still shows a repetitive roughness of 2 µm in height, the tracks remain homogenous and approximately 5.5 µm thick.

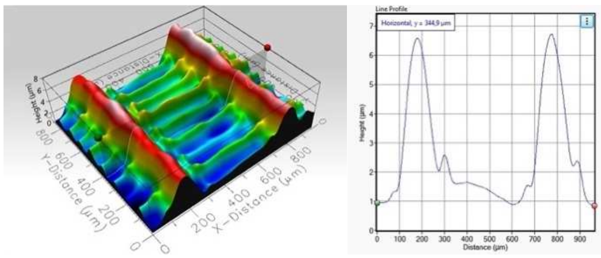

Fig. 5. Profilometry scan of one bending specimen with printed and sintered sensor. 3D view of two near track in the middle of the gauge grid (left) and a cut line drawn perpendicularly to them (right) showing height (µm) versus distance along the line (µm); resulting track width and height are visible.

B. *Flexural Tests*

In a 3-point bending test the beam is supported at two points which distance is the support span **L** and the force is applied at midpoint. So, from simple beam theory the bending momentum **M** at midpoint is:

$$M = \frac{FL}{4} \tag{1}$$

The strain gauge is placed at the outer surface **h/2** (with h being the beam thickness). The moment of inertia **I** is:

$$I = \frac{bh^3}{12} \tag{2}$$

Stress **σ** at midspan is:

$$\sigma = \frac{My}{I} \tag{3}$$

The commercial strain gauge has a GF of 2 as reported by manufacturer's datasheet. Strain measured by the strain gauge's relative resistance response $\Delta R/R_0$, where R_0 is the baseline resistance when no loading is applied, as follows:

$$\varepsilon = GF\frac{\Delta R}{R_0} \tag{4}$$

PLA beam's Young's flexural modulus E_F is calculated by this formula, given (3) and (4):

$$E_F = \frac{6FL}{bh^2\varepsilon} \tag{5}$$

Load vs strain curve was fitted linearly to find its slope and according to (5), Young's flexural modulus is 2.48 GPa. Maximum stress level of 17.3 MPa was found to be sufficiently below PLA's bending strength found in manufacturer's datasheet (76MPa). This way it was sure to be working in material's linear elastic regime.

Electrical resistance and strain level correlation of printed sensors was evaluated with 10 loading-unloading cycles as previously mentioned. This time strain was measured using load recordings and Young's flexural previously found modulus as follows:

$$\varepsilon = \frac{\sigma}{E_F} \tag{6}$$

Baseline resistance R_0 of the 9 non-embedded samples tested ranges from 25.8 to 74.6 Ω, so 4-wire measurement was employed. Relative resistance variation was correlated with strain by 1st order fitting. Sensitivity **S** was calculated using slope. Mean **S** across the 9 samples tested was found to be 0.87 ±0.12 (Ω/Ω)/ε with an R^2 of 0.98. This sensitivity cannot be confused with typical GF factor of strain gauges because sensor's geometry could influence resistance response during this type of tests. 3-point bending tests lead to a non-uniform stress distribution along the beam length. So, strain levels depend on the distance from the midpoint. This means that at sensor's center strain is maximum, and then it linearly decreases across its length. A gauge length of 6 mm is enough to show this effect and effectively lower sensor's sensitivity overall. So, the measured strain is not the peak but an average along gauge' grid length. These results though lead to assuming that printed sensors can sustain bending and show a linear and repeatable behavior. Fig. 6 shows one sample characterization curve $\Delta R/R_0$ vs estimated strain. During cycles the resistance variation remains linear and with same sensitivity to strain but drifts to lower values due to viscoelasticity of PLA. Ideally the effect should make the cycles stabilize, but in the 10 application it was not reached yet.

Sensitivity variation over different cycles of strain applied was tested on one sample. The 10 cycle of loading unloading used previously was repeated for 7 tests. In each test a different maximum force was applied to induce a different strain level on the outer surface where the sensor was printed; Fig. 7 shows the applied load during the 7 tests in the time domain. The resulting strain levels applied were measured using load recordings and Young's flexural modulus using (6) and were approximately 0.05%, 0.1%, 0.15%, 0.2%, 0.3%, 0.35% and 0.4%.

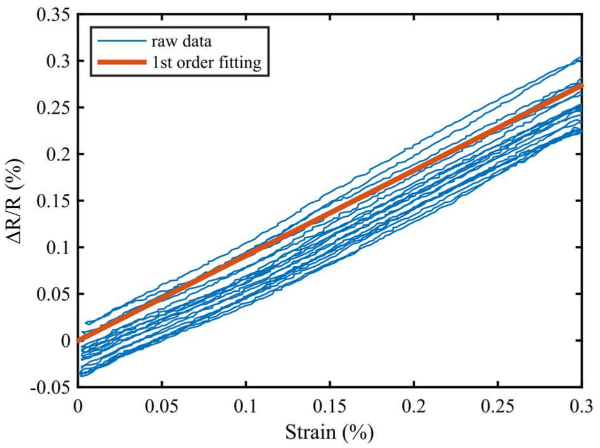

Fig. 6. Relative resistance change (%) versus strain (%) measured on the 9 test samples during 10 cycles of loading-unloading.

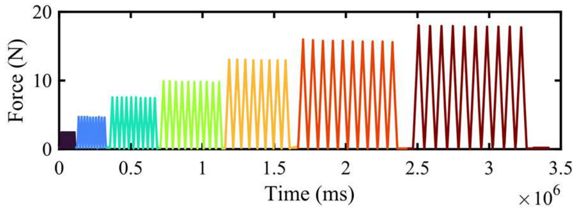

Fig. 7. Force (N) applied during 7 consecutive bending tests (different colours: 0.05%, 0.1%, 0.15%, 0.2%, 0.3%, 0.35% and 0.4%). Each test is 10 cycles long and reach an increasing strain level.

Resistance response was measured during these tests. Relative resistance over strain applied shows good linearity in every test, as reported in Fig. 8. Sensitivity was calculated by 1st order fitting and proved to be consistent, ranging from 0.71 and 0.86 (Ω/Ω)/ε. Viscoelastic effect is still visible in these tests and becomes more significant when strain applied is more than 0.2%.

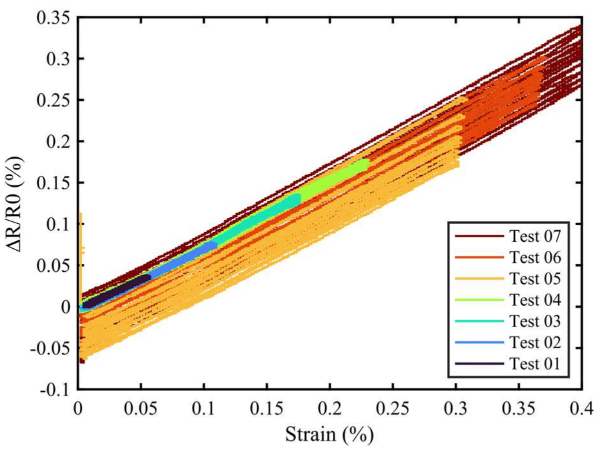

Fig. 8. Relative resistance change (%) over strain (%) applied to one sample for 7 tests (different colours: 0.05%, 0.1%, 0.15%, 0.2%, 0.3%, 0.35% and 0.4%). Each test is 10 cycles long, reaching a set strain level.

A stability test was then conducted on one sample. A deflection of -0.6 mm was applied to the beam and was hold for 10 minutes. The relative resistance changes to 0.31% at first and then lowers during time to 0.28%, as shown in Fig. 9, due to relaxation typical of viscoelastic materials such as PLA, known as creep and visible in previous tests as well. Although PLA's creep is out of the scope of this study, it's worth mentioning that in dynamic scenarios, such as gait analysis (which features oscillatory frequencies around 1-2 Hz), the slow time constants typical of polymeric viscoelastic relaxation would not have the physical time to significantly alter or corrupt the peak-to-peak amplitude of the electrical signal. This ensures transient measurements with a high signal-to-noise ratio, preserving the clinical utility of the device.

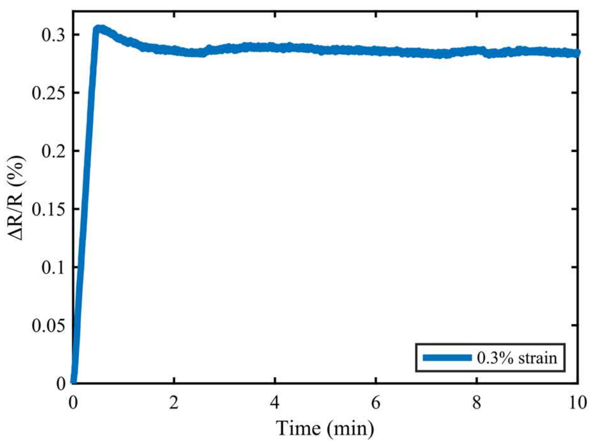

Fig. 9. Stability test conducted on a test sample. Relative resistance change over 10 minutes of sustained 0.3% strain application.

Same loading-unloading history as the first test described was applied to proof-of-concept samples, one for each encapsulation method presented previously. The resulting beam structure is different than pure flexural specimens used before, so force applied, and strain experienced at the surface are different. Electrical resistance response is not the same but, as Fig. 10 shows, it follows deflection application in time. Many effects could be causing this; firstly, the actual final geometrical shape of the embedded samples is not an ideal beam, so the equation proposed and used don't describe this structure; also, the embedding strategies employed could alter local stress and strain distribution. Although these effects will be part of future studies, this is enough to state that fabrication process was a success: sensors remained conductive and still sense strain.

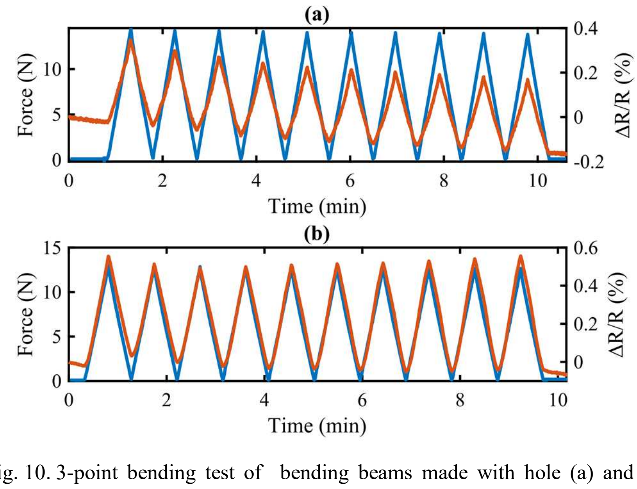

Fig. 10. 3-point bending test of bending beams made with hole (a) and kapton tape covering (b) methods of encapsulation. Relative resistance change (red) and force applied (blu) during 10 loading-unloading cycles.

IV. Conclusions

This preliminary study demonstrated the feasibility of embedding Aerosol Jet Printed (AJP) strain sensors inside FDM 3D-printed PLA structures using a commercially available desktop printer and a hybrid Print–Pause–Print (PPP) process. The integration of ironing as an in-process surface post-treatment proved essential to achieve a sufficiently smooth substrate for reliable AJP deposition. Surface roughness was reduced by approximately 89% compared to non-ironed surfaces, enabling homogeneous silver nanoparticle ink tracks with an average width of 200 µm and thickness of approximately 5.5 µm after photonic curing.

Flexural characterization confirmed that the printed strain sensors exhibit a linear and repeatable electrical response under bending. The mean sensitivity obtained from nine samples was 0.87 ± 0.12 $(\Omega/\Omega)/\varepsilon$, demonstrating consistent behavior across fabricated devices. Although the measured sensitivity reflects an average strain along the gauge length due to non-uniform stress distribution in 3-point bending, the results validate the capability of AJP-printed sensors to reliably transduce mechanical deformation on PLA substrates.

Most importantly, proof-of-concept fully embedded sensors remained conductive and responsive after encapsulation with additional PLA layers. Despite structural differences introduced by the embedding strategies, resistance variations consistently followed applied deflection, confirming the mechanical and electrical integrity of the hybrid manufacturing process. Both encapsulation approaches demonstrated process viability, highlighting practical considerations for future orthotic integration.

Future work will focus on optimizing sensor geometry and gauge factor under realistic orthotic loading conditions, improving encapsulation reliability, reducing viscoelastic drift effects through material selection, and integrating signal conditioning electronics. Validation on functional orthotic prototypes will be necessary to assess clinical applicability for gait analysis and rehabilitation monitoring.

V. Acknowledgements

This work has received funding from the European Union's Horizon Europe research and innovation programme under Grant Agreement No. 101136376 (SmILE – Smart Implants for Life Enrichment, HORIZON-HLTH-2023-STAYHLTH-01, CUP: D83C24001650006). Views and opinions expressed are however those of the author(s) only and do not necessarily reflect those of the European Union or the European Health and Digital Executive Agency (HaDEA). Neither the European Union nor the granting authority can be held responsible for them.

VI. References

[1] H. Atallah, T. Qufabz, H. R. Bakhsh, and G. Ferriero, "The current state of 3D-printed orthoses clinical outcomes: a systematic review," *BMC Musculoskelet. Disord.*, vol. 26, no. 1, p. 822, Sep. 2025, doi: 10.1186/s12891-025-09070-4.

[2] D. B. Devanand and A. E. Kedgley, "Objective Methods of Monitoring Usage of Orthotic Devices for the Extremities: A Systematic Review," *Sensors*, vol. 23, no. 17, p. 7420, Aug. 2023, doi: 10.3390/s23177420.

[3] A. Oarcea, F. Popister, P. Ciudin, and M. C. Salatioan, "Development of Smart Orthosis with Real-time Corrective Feedback," in *2023 17th International Conference on Engineering of Modern Electric Systems (EMES)*, IEEE, Jun. 2023, pp. 1–4. doi: 10.1109/EMES58375.2023.10171632.

[4] S. Mahraoui and M. Serpelloni, "Wireless Instrumented Ankle Foot Orthosis (AFO) for Gait Cycle Monitoring: a Preliminary Study," in *2025 IEEE International Workshop on Metrology for Industry 4.0 & IoT (MetroInd4.0 & IoT)*, IEEE, Jul. 2025, pp. 89–94. doi: 10.1109/MetroInd4.0IoT66048.2025.11122054.

[5] W. Svensson, T. Salomonsson, and U. Holmberg, "Foot orthosis strain sensing in hill walking," in *2007 IEEE 10th International Conference on Rehabilitation Robotics*, IEEE, Jun. 2007, pp. 700–703. doi: 10.1109/ICORR.2007.4428502.

[6] A. Tognetti, F. Lorussi, N. Carbonaro, and D. De Rossi, "Wearable Goniometer and Accelerometer Sensory Fusion for Knee Joint Angle Measurement in Daily Life," *Sensors*, vol. 15, no. 11, pp. 28435–28455, Nov. 2015, doi: 10.3390/s151128435.

[7] E. Papi, J. Maclean, R. J. Bowers, and S. E. Solomonidis, "Determination of loads carried by polypropylene ankle-foot orthoses: A preliminary study," *Proc. Inst. Mech. Eng. H*, vol. 229, no. 1, pp. 40–51, Jan. 2015, doi: 10.1177/0954411914566630.

[8] J. S. Dufek, E. S. Neumann, M. C. Hawkins, and B. O'Toole, "Functional and dynamic response characteristics of a custom composite ankle foot orthosis for Charcot-Marie-Tooth patients," *Gait Posture*, vol. 39, no. 1, pp. 308–313, Jan. 2014, doi: 10.1016/j.gaitpost.2013.07.121.

[9] A. Dijkshoorn *et al.*, "Embedded sensing: Integrating sensors in 3-D printed structures," *Journal of Sensors and Sensor Systems*, vol. 7, no. 1, pp. 169–181, Mar. 2018, doi: 10.5194/jsss-7-169-2018.

[10] C. Shemelya *et al.*, "Multi-functional 3D printed and embedded sensors for satellite qualification structures," in *2015 IEEE SENSORS*, IEEE, Nov. 2015, pp. 1–4. doi: 10.1109/ICSENS.2015.7370541.

[11] G. Stano, S. M. A. I. Ovy, J. R. Edwards, M. Cianchetti, G. Percoco, and Y. Tadesse, "One-shot additive manufacturing of robotic finger with embedded sensing and actuation," *The International Journal of Advanced Manufacturing Technology*, vol. 124, no. 1–2, pp. 467–485, Jan. 2023, doi: 10.1007/s00170-022-10556-x.

[12] M. S. Hassan *et al.*, "3D Printed Integrated Sensors: From Fabrication to Applications—A Review," *Nanomaterials*, vol. 13, no. 24, p. 3148, Dec. 2023, doi: 10.3390/nano13243148.

[13] D. Zhao, T. Liu, M. Zhang, R. Liang, and B. Wang, "Fabrication and characterization of aerosol-jet printed strain sensors for multifunctional composite structures," *Smart Mater. Struct.*, vol. 21, no. 11, p. 115008, Nov. 2012, doi: 10.1088/0964-1726/21/11/115008.

[14] J. F. Hernández-Rodríguez, D. Rojas, and A. Escarpa, "Print-Pause-Print Fabrication of Tailored Electrochemical Microfluidic Devices," *Anal. Chem.*, vol. 95, no. 51, pp. 18679–18684, Dec. 2023, doi: 10.1021/acs.analchem.3c03364.

[15] B. Neuhaus, M. K. Idris, P. Naderi, Y. El-Hajj, and G. Grau, "Low-Roughness 3D-Printed Surfaces by Ironing for the Integration with Printed Electronics," *Adv. Eng. Mater.*, vol. 26, no. 3, Feb. 2024, doi: 10.1002/adem.202301711.

[16] H. Alzyod and P. Ficzere, "Ironing process optimization for enhanced properties in material extrusion technology using Box–Behnken Design," *Sci. Rep.*, vol. 14, no. 1, Dec. 2024, doi: 10.1038/s41598-024-52827-5.